Slip velocity and stresses in granular Poiseuille flow via event-driven simulation

Vijayakumar Chikkadi and Meheboob Alam*
Engineering Mechanics Unit, Jawaharlal Nehru Centre for Advanced Scientific Research, Jakkur P.O., Bangalore 560064, India
(Received 18 March 2009; revised manuscript received 1 June 2009; published 12 August 2009)

Event-driven simulations of inelastic smooth hard disks are used to probe the slip velocity and rheology in gravity-driven granular Poiseuille flow. It is shown that both the slip velocity (U_w) and its gradient (dU_w/dy) depend crucially on the mean density, wall roughness, and inelastic dissipation. While the gradient of slip velocity follows a single power-law relation with Knudsen number, the variation in U_w with Kn shows three distinct regimes in terms of Knudsen number. An interesting possibility of Knudsen-number-dependent specularity coefficient emerges from a comparison of our results with a first-order transport theory for the slip velocity. Simulation results on stresses are compared with kinetic-theory predictions, with reasonable agreement of our data in the quasielastic limit. The deviation of simulations from theory increases with increasing dissipation which is tied to the increasing magnitude of the first normal stress difference ($\mathcal{N}_1$) that shows interesting nonmonotonic behavior with density. As in simple shear flow, there is a sign change of $\mathcal{N}_1$ at some critical density and its collisional component and the related collisional anisotropy are responsible for this sign reversal.

DOI: 10.1103/PhysRevE.80.021303 PACS number(s): 45.70.−n, 47.45.Gx, 47.57.Qk

I. INTRODUCTION

Granular materials, a collection of macroscopic particles, are ubiquitous in various chemical processing industries as well as in nature [1]. At rest, granular materials represent a dead state since the thermal energy of particles is negligible compared to their potential/interaction energy and hence they represent athermal system [2,3]. External energy must be feed in continuously to make granular materials to flow since the particle collisions are always dissipative. Depending on the strength of external energy, granular materials can be in any of the three well-known states of matter: gas, liquid, and solid. In the "quasistatic" regime of granular solid, the particle interactions are characterized by enduring frictional contacts with sliding and rolling motion dominating their interactions; in such dense slow flows, the deformation rates are low. The development of constitutive relations for such dense frictional flows has been mainly motivated by experiments and simulations [1]. Under strong external driving, a picture of granular materials in the "rapid" flow regime [2], a granular fluid, is reminiscent of molecular fluids, with particles moving around randomly. As in molecular fluids, particle collisions are assumed to be binary and instantaneous, with one major difference being the *inelastic* nature of collisions. It turns out that the "dissipation" of energy associated with inelastic collisions is responsible for a host interesting behavior in granular fluid.

One of the major challenges in granular flow research has been the continuum modeling of flowing granular materials [1–3]. The formulation of Navier-Stokes-type equations of motion for granular fluids has been an active area of research during the last two decades. The ideas of dense-gas kinetic theory have been extended to macroscopic "dissipative" particles to develop a theoretical understanding of the rapid granular flow [4]. The first attempt to derive constitutive equations for rapid granular flows from microscopic considerations, based on heuristic arguments, was made by Bagnold [5] who showed that, at reasonably large concentrations and shear rates, the stresses generated depend on the square of the imposed shear rate. Following Ogawa's idea, Haff [4] proposed a balance equation for the fluctuation energy using heuristic arguments drawing an analogy of particle motion with thermal motion in gases. Later, the constitutive equations were developed based on the formalism of kinetic theory [4]. Savage and Jeffrey [4] have developed constitutive relations for smooth, hard, and elastic spheres in a simple shear assuming Maxwellian velocity distribution function. Their results showed a good agreement with the experimental results of Bagnold [5]. Since the balance equation for energy was not considered, they could not predict the temperature. In the next step, Jenkins and Savage [4] solved the energy balance equation for the granular temperature assuming Maxwellian distribution as the single particle velocity distribution and using an approximate linear anisotropic pair distribution function valid only in the elastic limit. Based on the observation that in the double limit of inelasticity ($\epsilon=1-e_n^2$, where e_n is the normal coefficient of restitution) and Knudsen number (Kn) approaching zero, the collisionally relaxed state corresponds to a Maxwellian, Sela and Goldhirsch [4] proposed a modified Chapman-Enskog expansion in which both ϵ and Kn are small parameters. Most of these models [4] hold for nearly elastic collisions ($e_n \sim 1$) and have been reasonably successful in describing the fluidized and quasielastic regimes, but fail to explain the whole range of behavior of granular flows, especially at large dissipations and dense flows. Under such circumstances, discrete particle simulations could be very helpful in validating various continuum models and also establishing their range of validity.

While the rheology of uniform shear flow of dry granular materials has been extensively studied via simulation and theory [2], similar studies on prototypical inhomogeneous

*Author to whom correspondence should be addressed; meheboob@jncasr.ac.in

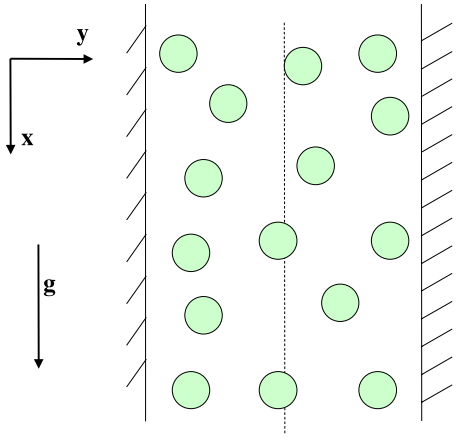

FIG. 1. (Color online) Schematic of granular Poiseuille flow.

flows (e.g., Poiseuille-type flows) are relatively scarce. Both the single particle statistics and the bulk behavior of the gravity-driven "granular" Poiseuille flow (GPF) through a channel have been probed via experiments [6] and simulations [7–10]. Most simulations on GPF dealt with probing the large-scale density waves [7,8] and single particle statistics [9]; stresses as well as jamming transition in "dense" GPF have also been probed via simulations [10]. In contrast, however, the *rheology* of GPF in the *rapid* flow regime, spanning a wide range of densities from the dilute to dense flows, has not been probed systematically; moreover, there is hardly any information on the *slip velocity* in GPF. The above two issues are the focus of the present paper.

In this paper we consider the granular Poiseuille flow which is the gravity-driven flow of granular materials [8,9], focusing on the "rapid" flow regime. We use event-driven simulations of inelastic smooth hard disks to model flowing granular particles in a two-dimensional channel bounded by two frictional walls. In the first part, we study slip velocity in GPF as a function of density, inelasticity, and wall roughness and identify power-law relations for slip velocity and its gradient with Knudsen number. In the second part, we probe various rheological quantities and make a systematic comparison with kinetic-theory constitutive models [11]. Apart from particle pressure, shear viscosity, and shear stress, a quantity of particular interest is the first normal stress difference ($\mathcal{N}_1$), which is a measure of the non-Newtonian character of granular fluid. Here we quantify this non-Newtonian effect in GPF and its possible connection with Burnett-order phenomenon [12] and collisional anisotropy [13] is carefully probed. For the latter part, we follow the work of Alam and Luding [13–15] to analyze the behavior of $\mathcal{N}_1$ in GPF over a large range of densities and show that the sign reversal of $\mathcal{N}_1$ in GPF can occur even at a modest density (much lower than that in the simple shear flow).

II. SIMULATION METHOD

The simulated system is a channel of length L along the periodic x direction and bounded by two plane solid walls, parallel to the x direction, with a separation of width W (along the y direction) as shown in Fig. 1. The granular material, consisting of N identical rigid and smooth disks of equal mass m and diameter d, is driven by gravity along the x direction. The interactions that are allowed are instantaneous "dissipative" collisions between pairs of particles and between a particle and the walls. An event-driven algorithm [16] is used to simulate the evolution of particles in time. The dissipative nature of particle collisions is characterized by the coefficient of normal restitution, e_n, which is given by the following expression:

$$\mathbf{k}\cdot\mathbf{c}'_{21} = -e_n(\mathbf{k}\cdot\mathbf{c}_{21}), \tag{1}$$

where $\mathbf{c}_{21}$ and $\mathbf{c}'_{21}$ are precollisional and postcollisional relative velocities and $\mathbf{k}$ is the unit vector directed along the line connecting the centers of particle 2 and particle 1. There is no relative tangential velocity since the particles are assumed to be *smooth*.

A. Model for frictional wall

The solid walls are modeled as frictional surfaces and a particle colliding with a wall is analogous to a particle colliding with a particle of infinite mass moving at the velocity of the wall. A single parameter, *coefficient of tangential restitution* for particle-wall collisions β_w, has been used to model the frictional properties of walls [8,9]. It is defined as the average fraction of relative tangential momentum transmitted from a particle to the wall during a particle-wall collision. The collision rule of a particle-wall collision is given by

$$c'_x = \beta_w c_x \quad \text{and} \quad c'_y = -e_w c_y, \tag{2}$$

where e_w is the normal restitution coefficient for particle-wall collisions; we have set $e_w=1$ for all results presented in this paper. The wall roughness is controlled by choosing a specific value of β_w: $\beta_w=1$ corresponds to a perfectly *smooth* wall for which the tangential velocity of particle remains same upon a particle-wall collision; $\beta_w=0$ corresponds to a *rough* wall for which the dissipation of energy at walls is maximum and there is no relative tangential slip between the particle surface and the wall upon a wall-particle collision; $\beta_w=-1$ corresponds to a perfectly *rough* wall for which the tangential velocity of particle *reverses* upon a particle-wall collision. The last condition with $e_w \neq 1$ is the analog of the well-known "bounce-back" scheme which is routinely used to mimic no slip in MD simulations of Newtonian fluids.

B. Averaging method and control parameters

Since the mean fields of GPF vary across the wall normal (y) direction, all the statistics presented in this paper were computed *binwise* by dividing the channel into several bins along the y direction; the width of each bin was chosen to be slightly larger than the diameter of a particle. The method of averaging followed for computing macroscopic properties of mean flow is given below:

$$C_i(t) = c_i(t) - U_x(y_i,t), \tag{3a}$$

$$U_x(y_i,t) = \frac{1}{N_y}\sum_{N_y}^{i=1} c_{xi}(t)\,\delta(y-y_i), \tag{3b}$$

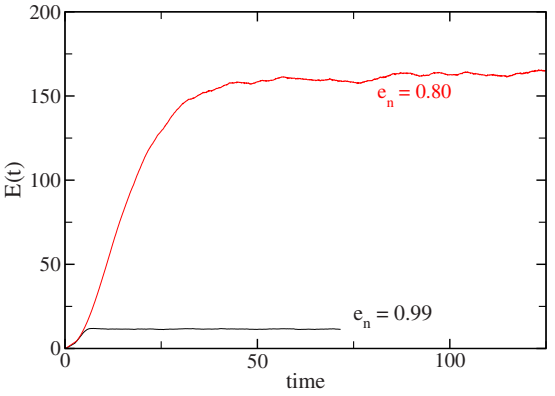

FIG. 2. (Color online) Temporal evolution of average kinetic energy per particle, $E(t)=(1/2N)\Sigma_{i=1,N}[c_{xi}(t)^2+c_{yi}(t)^2]$, for $\nu=0.56$, $W/d=31$, $N=900$, and $\beta_w=0.9$. $E(t)$ has have been rescaled by gW.

$$U_x(y) = \langle U_x(y_i,t)\rangle, \tag{3c}$$

$$\nu(y) = \frac{\pi}{4}d^2\left\langle \frac{1}{A_y}\sum_{N_y}^{i=1} \delta(y-y_i)\right\rangle, \tag{3d}$$

$$T(y) = \left\langle \frac{1}{N_y}\sum_{N_y}^{i=1} C_i(t)C_i(t)\delta(y-y_i)\right\rangle, \tag{3e}$$

where $c_i(t)$ is the instantaneous velocity of the ith particle, $C_i(t)$ is the fluctuating/peculiar velocity of the particle, $U_x(y_i,t)$ is the instantaneous mean velocity in the bin corresponding to the position y_i of the particle, N_y is the number of particles in ith bin, A_y is the bin area, and $\langle\cdots\rangle$ represents a time average. Analogous to molecular gases, the random velocity associated with granular particles is used to define the granular temperature T in Eq. (3e). Other properties of interest are defined in a similar way.

For time averaging, the data are collected in each bin over a large number of collisions once the flow has reached a steady state (see Fig. 2). The number of collisions considered for computing rheological quantities and slip velocity was around 10 000 per particle which was found to be sufficient. For the same flow configuration, the simulation code has been validated and some results on velocity distribution functions have been recently published [9].

There are five control parameters in this problem: the average volume fraction of particles (ν), the coefficient of normal restitution (e_n), the wall roughness (β_w), the channel width (W/d), and the channel aspect ratio (L/W). The mean/average volume fraction,

$$\nu = \pi N/4(L/W)(W/d)^2, \tag{4}$$

can be varied by changing the total number of particles (N) or the physical dimensions of the system (W/d and L/W). In the present simulation, we have fixed particle diameter d at unity, $N=900$ and $W/d=31$ and varied the channel length (L/W) to change the average volume fraction.

C. Steady GPF

In granular Poiseuille flow, the energy loss due to particle-particle and particle-wall collisions compensates the work done by the body force (gravity) after long enough time, leading to a steady state for any dissipation level ($e_n<1$) and wall roughness ($\beta_w<1$). This is in contrast to the gravity-driven Poiseuille flow of *elastic* ($e_n=1$) particles with smooth walls ($\beta_w=1$) for which a *thermostat* [17,18] is needed to attain a steady state with parabolic velocity profile. For *dissipative* particles, the inelastic dissipation and/or wall roughness plays the role of a thermostat.

The statistical steady state of GPF was ascertained by monitoring the temporal evolution of the average kinetic energy (per particle) which reached some constant value after initial transients; see Fig. 2. At the steady state $[\partial/\partial t(\cdot)=0]$ of fully developed $[\partial/\partial x(\cdot)=0]$ GPF, the profiles of the streamwise velocity $[U_x/U_0$, where U_0 is the velocity at $y=0]$, the density (ν), and the granular temperature (T) have spatial variations only along the wall-normal direction; see Figs. 3(a) and 3(b). Note that the local density is maximum at the channel centerline (and the granular temperature is minimum at $y=0$) at any value of e. The density variation across y is small in the quasielastic limit ($e_n\to 1$) but increases with increasing dissipation (i.e., with decreasing e_n) leading to a *plug* flow. At $e_n=0.8$, most of the particles migrate toward the channel centerline forming a dense plug with dilute regions residing near two walls. An example of plug formation can be visualized from two movies [19] given in supplementary materials (movie 1 for $e_n=0.99$ and movie 2 for $e_n=0.8$ at $\nu=0.56$).

Lastly, we make comments about possible effects of clustering and our choice of channel width $W/d=31$ in these simulations. Plug formation as observed in movie 2 [19] is an example of *clustering* that appears with increasing dissipation for any W/d; however, other types of clustering can also occur in GPF. For example, if the channel width is large, along with large dissipation levels ($e_n\ll 1$), the plug-type GPF becomes unstable [8] to axial perturbations leading to two types of density waves: *sinuous waves* and *clumps* or *slugs*. For both cases, the density field (as well as other mean fields) has considerable variation along the axial direction (i.e., $\nu\equiv\nu(x,y)$ and $\partial\nu/\partial x\neq 0$). The onset of such density waves in GPF and their dependence on various control parameters have been thoroughly characterized by Liss *et al.* [8] using event-driven simulations of the same collision model. They showed that if the channel width is small enough ($W/d<35$), such *axially inhomogeneous* density waves do not appear (see the phase diagram in Fig. 8 of Ref. [8]). In present simulations, our choice of a relatively narrow channel ($W/d=31$) was made to minimize the possibility of the appearance of density waves having axial variation. (Had we allowed axially inhomogeneous density waves by choosing a wider channel, we would have to go for *cellwise* averaging method, i.e., by dividing the channel into a number of rectangular cells to calculate any quantity.) In all our simulations at any mean density (with $W/d=31$ and $N=900$), the plug formation (i.e., $\nu\equiv\nu(y)$ as in movie 2 [19]) was found to occur for $e_n\geq 0.85$; but axially inhomogeneous density waves started to appear for $e_n\leq 0.80$ at intermediate values

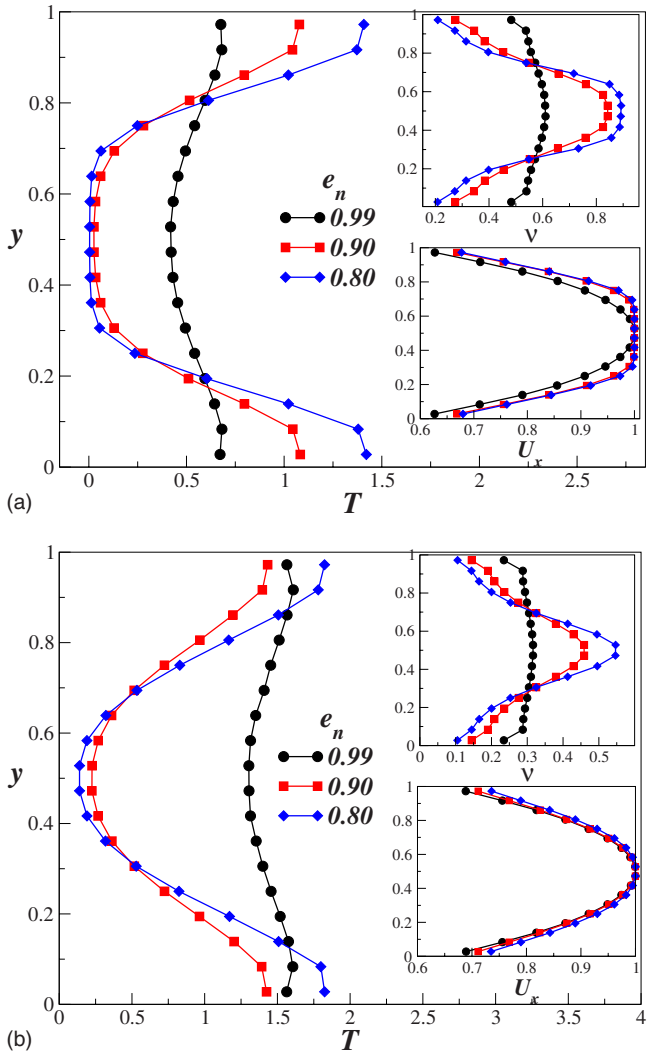

FIG. 3. (Color online) Profiles of granular temperature (main panel), particle volume fraction (upper inset), and streamwise velocity (lower inset) for (a) $\nu=0.56$ and (b) $\nu=0.3$. Other parameters as in Fig. 2. Note that the velocity has been rescaled by its centerline value, $U_x \equiv U_x/U_x(y=0)$, and the granular temperature by gW.

of mean density $[\nu \sim (0.2-0.4)]$. Here onward, we will not dwell on clustering/density waves (which is not the focus of this paper), but interested readers may consult Ref. [8] for any detail on this topic.

III. KNUDSEN NUMBER AND SLIP VELOCITY IN GRANULAR POISEUILLE FLOW

The boundary conditions at a fluid-solid interface have been widely debated, and, traditionally, in continuum analysis no-slip condition at a fluid-solid interface is imposed [20,21]. But it has been confirmed by numerous experimental and numerical work that fluids indeed exhibit finite slip at walls. The magnitude of slip though depends on various factors such as the length scale of the flow, surface roughness, hydrophobicity, etc., and also on the nature of the fluid, whether a Newtonian/non-Newtonian liquid or a gas [21]. Gas flows show significant slip when the Knudsen number, which is defined as the ratio of mean free path of the gas molecules to the characteristic length of the flow, is large. The possibility of slip for an ideal gas was first addressed by Maxwell [20]; by assuming a combination of *specular* and *diffuse* types gas-wall collisions, he estimated the slip length for a rarefied gas.

Similar to microscale gas flows [21], the granular flows are known to be associated with considerable amount of slip at walls [22–24] and the magnitude of slip velocity depends on Knudsen number, restitution coefficients, particle volume fraction, and wall roughness. Before investigating the Knudsen number and slip velocity relation in Sec. III B, first we study the effect of different control parameters on Knudsen number in Sec. III A.

A. Knudsen number

In the present context, Knudsen number is defined as $\mathrm{Kn}=\lambda/W$, where the mean free path $\lambda=\langle s \rangle$ is computed by averaging particle displacements during successive collisions ($s=\sqrt{\delta x^2+\delta y^2}$, where δx and δy are the components of the instantaneous *free path* of two colliding particles, scaled by the particle diameter) over a large number of particle collisions, and W is the channel width. Since our flow is inhomogeneous across the channel width, Kn varies across the channel width; thus, the results presented below correspond to the average value of Kn for a given flow condition.

Figures 4(a) and 4(b) show the effect of inelastic dissipation (e_n) on Knudsen number and the probability distribution of particle displacements, respectively, at a wall roughness of $\beta_w=0.1$ (i.e., rough wall). The results in Fig. 4(a) are presented for different mean particle volume fractions (ν), and those in panel (b) are for different e_n at $\nu=0.4$. While the Knudsen number is found to increase with increasing dissipation in the dilute limit, it varies nonmonotonically with e_n for denser flows with its maximum attaining at around $e_n \sim 0.9$. Following the classification of flow in terms of Knudsen number [21], we find that the present flow is in the *transitional-flow* regime ($0.1<\mathrm{Kn}<10$) at low densities, but in the *slip-flow* regime ($0.01<\mathrm{Kn}<0.1$) at moderate densities. From the distribution of particle displacements $P(s)$ in Fig. 4(b), it is seen that $P(s)$ is almost an exponential for nearly elastic collisions ($e_n=0.99$). This behavior is similar to that for a molecular gas for which it can be proved that the probability distribution of free paths is an exponential [25]. At larger dissipations, the distribution function $P(s)$ deviates from an exponential for smaller values of displacements (s), however, the tail of $P(s)$ still follows an exponential decay at any e_n. The nonexponential decay of $P(s)$ for small s could be a signature of particle clustering that occurs at large dissipations.

In Figs. 5(a) and 5(b) the effect of wall roughness (β_w) on Knudsen number and the probability distribution of particle displacement are shown, respectively. In general, Kn decreases with increasing wall roughness (i.e., decreasing β_w) at any density. It is observed that the wall roughness has an appreciable effect for dilute flows ($\nu=0.015$) but has negligible effect at moderate densities ($\nu=0.3$) except for nearly elastic collisions. The former behavior could also be inferred

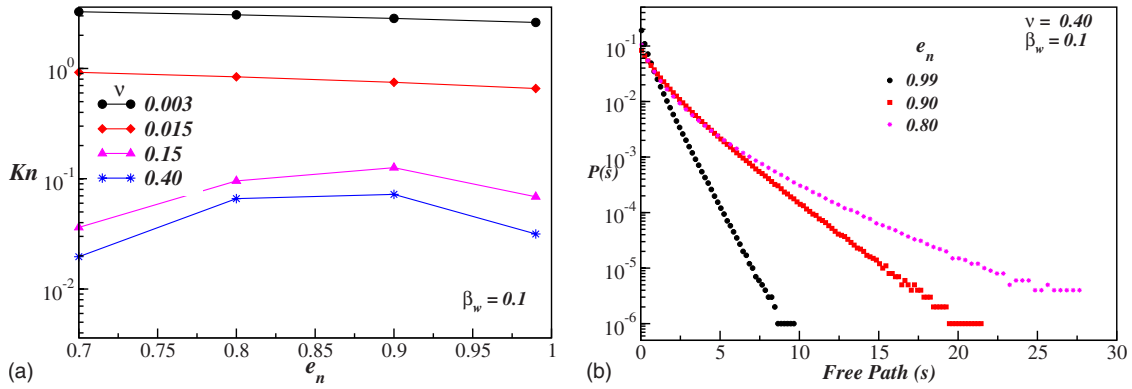

FIG. 4. (Color online) Effect of restitution coefficient (e_n) on (a) Knudsen number and (b) the distribution of particle displacement for a rough wall (β_w=0.1).

from the plot of $P(s)$ in Fig. 5(b) at ν=0.015. Note that the tail of $P(s)$ follows an exponential decay at any value of β_w.

Figure 6 shows that Knudsen number decreases with increasing particle volume fraction (ν) since the particles have lesser free areas to move around as the density is increased. For e_n=0.99 and 0.9, there seems to be a power-law behavior for Kn with ν, $\mathrm{Kn} \propto \nu^{-\alpha}$, over a range of mean density [$\nu \in (0.003-0.35)$]; for larger densities ($\nu > 0.4$), Kn decreases sharply. For more dissipative collisions ($e_n \leq 0.8$), the variation in Kn with density becomes nonmonotonic and does not follow a power law. As mentioned in Sec. II C, the density waves/clusters become significant at low $e_n(\leq 0.8)$, making the flow inhomogeneous in the whole domain, and the observed nonmonotonicity could be a consequence of such particle clustering.

B. Slip velocity and its gradient

Since the walls are stationary, the mean streamwise velocity of particles in each bin adjacent to walls, $U_x(y_i = y_{wbin})$ as defined in Eq. (3c), is the *slip velocity*. In the following, we define the nondimensional slip velocity as the ratio of the average velocity in the bins adjacent to two walls (U_w) and the centerline velocity (U_0).

Figures 7(a) and 7(b) show the combined effects of restitution coefficient e_n and mean particle volume fraction ν on the slip velocity (U_w) and its gradient (dU_w/dy), respectively, at a wall roughness of β_w=0.1 (i.e., rough wall). The inelastic dissipation does not seem to have a noticeable effect on both the slip velocity and its gradient, but they depend strongly on mean density.

Figures 8(a) and 8(b) show the effect of wall roughness (β_w) on slip velocity (U_w) and the streamwise velocity profiles. The parameter values used in Fig. 8(a) are e_n=0.99 and ν=0.015 and 0.30, and are e_n=0.99, ν=0.015, and β_w=0.1, 0.5 and 0.9 in Fig. 8(b). As expected, the slip velocity increases with increasing wall smoothness (that increases with increasing β_w) and vice versa as seen in Fig. 8(a), which is also evident from the velocity profiles in Fig. 8(b). Note that the velocity profile becomes more uniform across the channel width as the walls are made more smoother by increasing β_w. The slip-velocity gradient, dU_w/dy, (not shown) is found to decrease with increasing β_w for $\beta_w > 0$ and it depends strongly on mean volume fraction (see below).

The effects of mean volume fraction (ν) on the slip velocity and its gradient are shown in Figs. 9(a) and 9(b), respectively; the corresponding streamwise velocity profiles are shown in Fig. 9(c). While the slip velocity deceases with increasing volume fraction, the gradient of slip velocity increases in the same limit. This overall trend holds at other values of wall roughness β_w. It is observed from Fig. 9(b) that there is a power-law behavior for dU_w/dy with ν for the whole range of $\nu \in (0.003, 0.6)$ studied. In contrast, however,

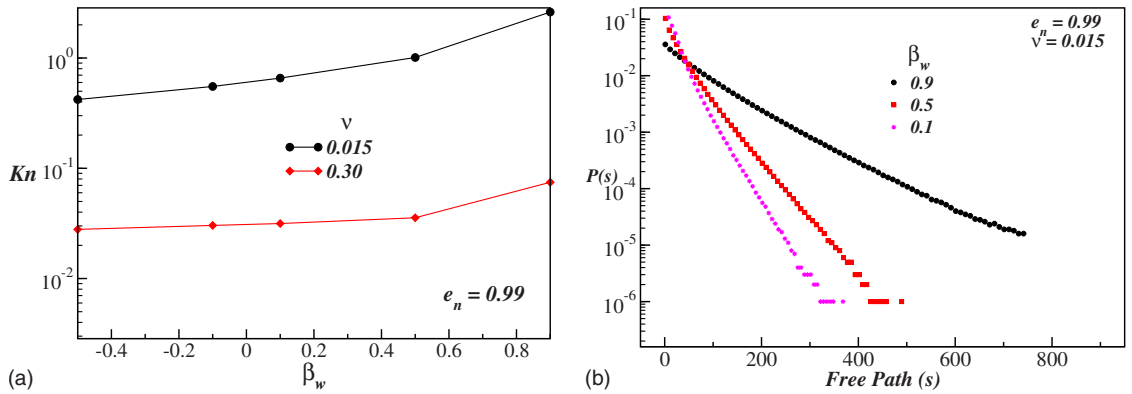

FIG. 5. (Color online) Effect of wall roughness (β_w) on (a) Knudsen number and (b) the distribution of particle displacement for e_n =0.99.

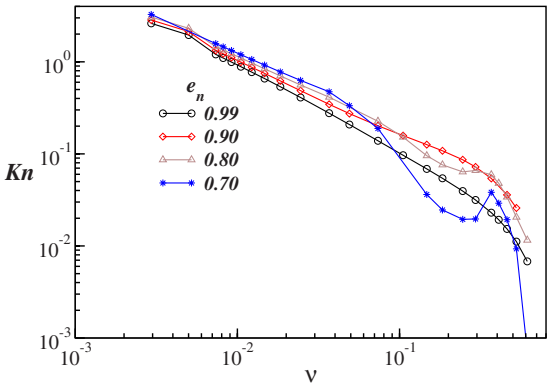

FIG. 6. (Color online) Effect of particle volume fraction (ν) on Knudsen number for a rough wall (β_w=0.1).

the variation in slip velocity with mean density cannot be described by a single power-law exponent (and there is a weak dependence on e_n too), especially the data for very dilute flows ($\nu<0.02$) and dense flows ($\nu<0.4$) have different variations with ν.

Since the Knudsen number is a strong function of the mean density (Fig. 6), the above variations in slip velocity and its gradient with density, as depicted in Figs. 9(a) and 9(b), can be directly translated into their variations with the Knudsen number as we will discuss below.

Figure 10(a) shows the variation in slip velocity with Knudsen number for a rough wall (β_w=0.1) for different values of e_n. In the main panel of Fig. 10(a) the black curve represented by open circles was computed using N=1800 and W/d=31, and there is a good agreement with the results obtained with N=900 and W/d=31 (filled circles). It is observed from the inset of Fig. 10(a) that the slip velocity can be fitted via a power law,

$$\frac{U_w}{U_0} \propto \mathrm{Kn}^{\alpha_1}, \tag{5}$$

over a decade of Kn$\sim$(0.05–1) for e_n=0.99 and 0.9. [The corresponding range of particle volume fractions was found to vary from moderate to very dilute values $\nu\sim$(0.4–0.02); see the inset of Fig. 9(a).] It is worth pointing out that for large dissipations ($e_n\leq 0.8$) the slip velocity becomes a nonmonotonic function of e_n for Kn$\leq$0.2, and hence the above power law (5) is strictly valid only for quasielastic collisions $e_n\geq 0.9$. Note that the exponent α_1 in Eq. (5) is a decreasing function of e_n: for example, $\alpha_1(e_n)$=0.57 and 0.75 for e_n =0.99 and 0.9, respectively.

For large Knudsen numbers (Kn$>$1), it is seen from the inset of Fig. 10(a) that the power-law exponent, $\alpha_1\approx 0.16$, is much lower than that for the intermediate range of Kn and this appears to be independent of the restitution coefficient e_n (note that the number of data points for Kn$>$1 is rather limited). For the other limit of low Knudsen numbers (Kn $<$0.05), our data for slip velocity [inset of Fig. 10(a)] seem to plateau to a constant value, i.e., $\alpha_1\approx 0$, irrespective of the value of e_n.

Figure 10(b) shows the variation in the gradient of slip velocity, dU_w/dy, with Knudsen number for a rough wall (β_w=0.1). From the inset of Fig. 10(b), we find that there is an excellent collapse of data for dU_w/dy over two decades of Kn for three values of restitution coefficients e_n=0.99, 0.9, and 0.8. The slip velocity gradient varies as a negative power of Knudsen number,

$$\frac{d}{dy}\left(\frac{U_w}{U_0}\right) \propto \mathrm{Kn}^{-\alpha_2}, \tag{6}$$

with an exponent of $\alpha_2\approx 0.21$ which is found to be independent of e_n.

From the above two scaling relations (5) and (6), a linear relation between the slip velocity U_w and its gradient dU_w/dy can be constructed (see discussion in Sec. III C):

$$U_w \propto \mathrm{Kn}^{\gamma}\frac{dU_w}{dy}, \tag{7}$$

with

$$\gamma(e_n) = \alpha_1(e_n) + \alpha_2. \tag{8}$$

Our data suggest a dependence of this exponent γ on the range of Knudsen number. For example, (i) in the regime of low Knudsen numbers (Kn$<$0.05) this exponent is

$$\gamma = \alpha_1 + \alpha_2 \approx 0.21,$$

(ii) in the regime of large Knudsen numbers (Kn$>$1)

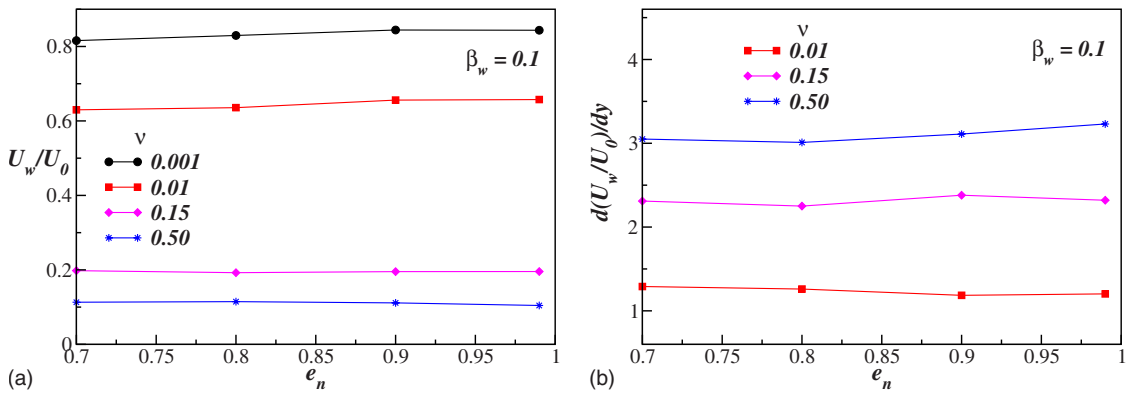

FIG. 7. (Color online) Effects of restitution coefficient (e_n) and density (ν) on (a) slip velocity (U_w) and (b) dU_w/dy. The wall roughness is set to β_w=0.1 (i.e., rough wall).

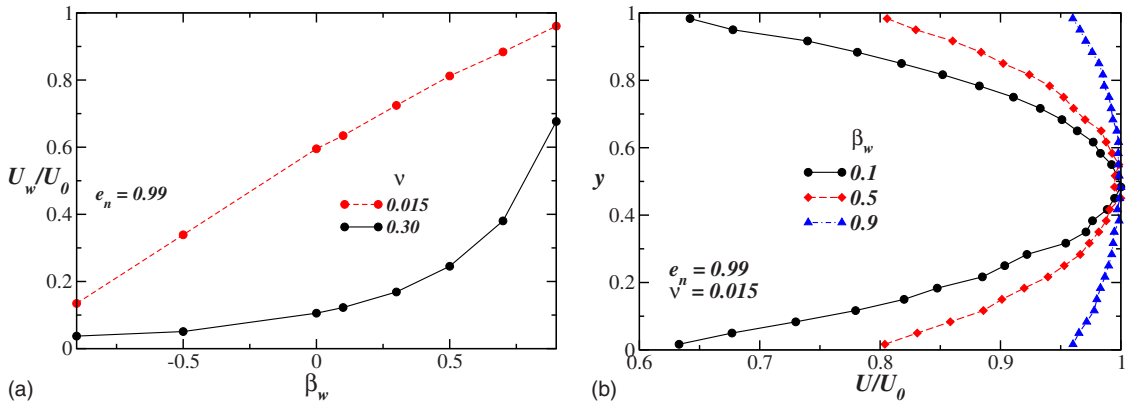

FIG. 8. (Color online) Effects of wall roughness (β_w) on (a) slip velocity (U_w) and (b) the streamwise velocity. The restitution coefficient is set to e_n=0.99 for all plots and the streamwise velocity in panel c is calculated at ν=0.015.

$$\gamma = \alpha_1 + \alpha_2 \approx 0.37,$$

and (iii) in the regime of intermediate Knudsen numbers $(0.05 < \mathrm{Kn} < 1)$

$$\gamma(e_n) = \alpha_1(e_n) + \alpha_2 \approx \begin{cases} 0.78 & (e_n = 0.99) \\ 0.96 & (e_n = 0.9). \end{cases}$$

In summary, while the gradient of slip velocity in GPF follows a single power-law relation with Knudsen number for the range of Knudsen numbers studied $\mathrm{Kn} \in (0.01, 3)$, the variation in slip velocity with Knudsen number reveals three different regimes in terms of Kn. Although the validity of a power law for U_w just over a decade of Kn [see inset of Fig. 10(a)] is questionable, here our emphasis is on the observation that U_w has different variations in three regimes of Kn: (i) $\mathrm{Kn} < 0.05$, (ii) $0.05 < \mathrm{Kn} < 1$, and (iii) $\mathrm{Kn} > 1$. The slip velocity and its gradient can be fitted to a linear relation with a Knudsen-number-dependent proportionality constant, Eq. (7). Since the Knudsen number has been varied by varying the mean density and dissipation in our simulations, the above proportionality constant (Kn) also depends indirectly on the mean density and other control parameters. In the

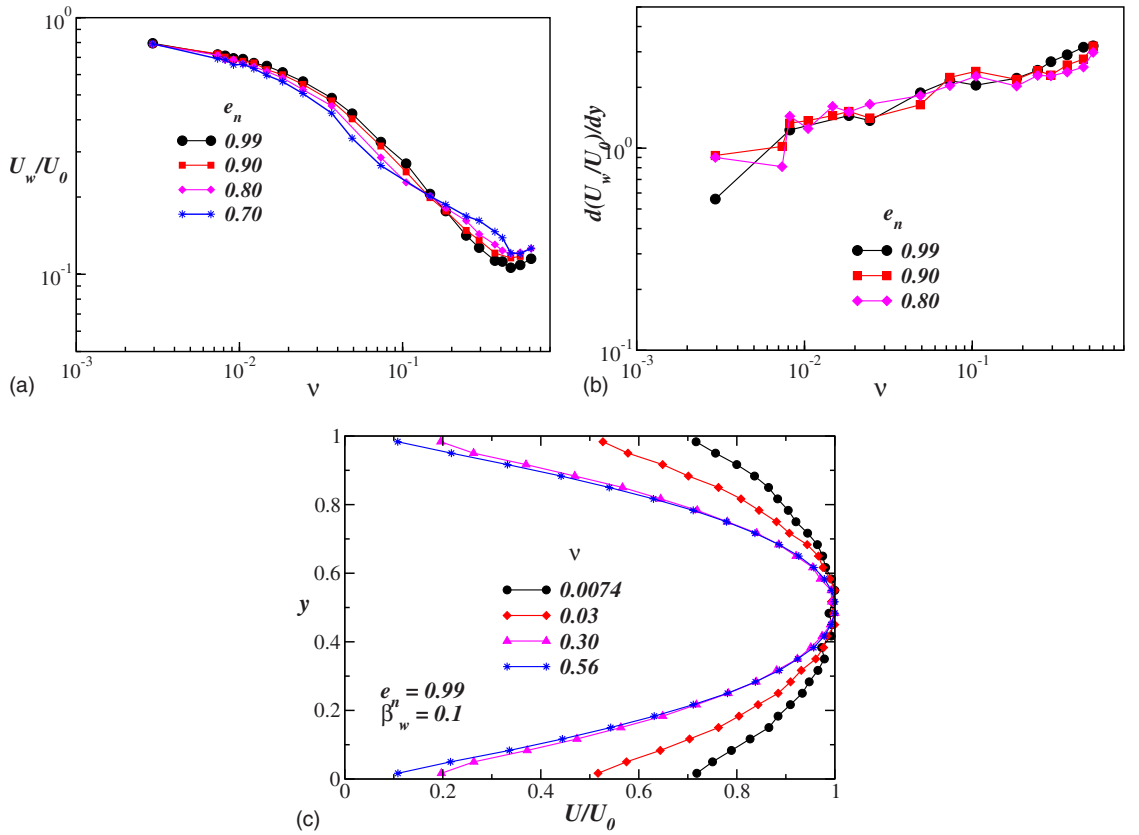

FIG. 9. (Color online) Effects of mean particle volume fraction (ν) on (a) slip velocity (U_w), (b) dU_w/dy, and (c) the streamwise velocity. The wall roughness is set to β_w=0.1 for all plots and the streamwise velocity in panel c is calculated at a restitution coefficient e_n=0.99.

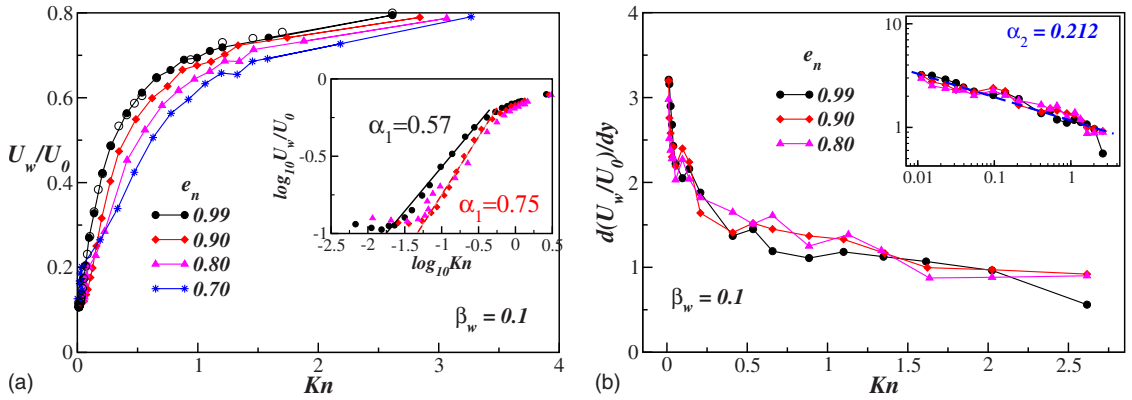

FIG. 10. (Color online) Variations in (a) the slip velocity and (b) the gradient of slip velocity with Kn at a wall roughness of β_w=0.1 and different values of dissipation. In panel (a), the open circles were computed for N=1800 particles at e_n=0.99. The inset in each panel shows the information of the main panel on a log-log scale and the related power-law exponents are also indicated.

following section, we seek a possible theoretical justification of this slip boundary condition.

C. Comparison with theory

Here we follow the heuristic transport theory of Hui *et al.* [22] to determine an expression for the slip velocity. If the mean velocity of particles near the wall differs from the wall velocity, there is a flux of momentum to the wall due to particle-wall collisions. In an averaged sense, this momentum flux to the wall is the product of three terms: (i) the collisional impulse per wall-particle collision, (ii) the collision frequency of wall-particle collision, and (iii) the number density of particles near the wall. Equating this wall-momentum flux along the direction of the wall with the bulk shear stress of granular fluid near wall, we obtain the following boundary condition for the slip velocity:

$$U_w = a(\nu)\left(\frac{\mathrm{Kn}}{\phi}\right)\frac{dU_w}{dy}, \tag{9}$$

where $a(\nu)$ is a function of particle volume fraction and ϕ is the *specularity* coefficient for particle-wall collisions which is a measure of the "large-scale" roughness of the wall. For a rough wall, the collisions are *diffuse* (i.e., the particles are deflected in random directions uncorrelated with their approaching direction) and the specularity coefficient is ϕ=1 resulting in a small slip velocity. For a smooth wall, the particles are deflected without any change in their tangential momentum for which ϕ=0 resulting in a large slip velocity.

Note that the predicted boundary condition, Eq. (9), is a "first-order" correction [20,21] to the well-known *no-slip* boundary condition and is strictly valid in the regime of low Knudsen number (Kn$\leq$0.01). In the regimes of slip and transitional flows (0.01$<$Kn$<$1), the linear relation [Eq. (9)] still holds but with an additional correction term proportional to the second derivative of slip velocity [21].

Leaving aside the correct form of velocity boundary conditions at large Knudsen number, we now return to our proposed scaling relation (7) which can be compared with the analytical relation (9) if we rewrite Eq. (7) as

$$U_w \propto \left(\frac{\mathrm{Kn}}{\phi(\mathrm{Kn})}\right)\frac{dU_w}{dy}, \tag{10}$$

where the specularity coefficient, ϕ(Kn), is now allowed to depend on Knudsen number. In contrast, however, the specularity coefficient is taken to be a *constant*, independent of any flow parameter, in most theoretical models of granular boundary conditions [22–24]. (Ideally, the specularity coefficient ϕ is tied to the wall geometry and the related wall-particle collision parameters as in the kinetic-theory treatment of boundary conditions.) Since both Knudsen number and slip velocity are found to depend on the particle volume fraction (ν), the wall-particle tangential restitution coefficient (β_w, i.e., "microscopic" or "small-scale" roughness) and normal restitution coefficient (e_n), the large-scale roughness of the wall (ϕ) would therefore depend on Kn. It would be interesting to determine the correct functional relation for the specularity coefficient $\phi(\mathrm{Kn};\beta_w,e_n,\ldots)$. A comprehensive justification of our proposed boundary condition, Eq. (10), requires a full kinetic-theory treatment of wall-particle collisions and the solution of Boltzmann-Enskog equation in the half-space which is beyond the scope of the present paper.

However, from our simulation data we can check our proposal about the Knudsen-number-dependent specularity coefficient if we know the correct form of $a(\nu)$ in Eq. (9). Focusing on the dense limit ($\nu\to\nu_m$, where ν_m is the maximum packing density) of low Knudsen number, we find that $a(\nu)\sim\nu$ [22,23]. From our data in Fig. 6, we have Kn $\sim\nu^{-\alpha}$, with the exponent α being unknown since we have only few data points in the dense limit (but a very crude estimate is $\alpha\approx$1.5 for e_n=0.99 and 0.9). Therefore, $a(\nu)$ $\sim\mathrm{Kn}^{-1/\alpha}$ which can be plugged into Eq. (9) and compared with Eqs. (7) and (10), leading to $\phi(\mathrm{Kn})\sim\mathrm{Kn}^{1-\gamma-1/\alpha}$. With γ=0.21(Kn$<$0.05) and α=1.5, we find $\phi(\mathrm{Kn})\sim\mathrm{Kn}^{0.123}$ that shows a weak dependence on Kn. On the other hand, ϕ(Kn) is a constant if $\alpha=(1-\gamma)^{-1}$. We hope these results would be useful to facilitate further comparison to any future theory and would motivate further simulations.

IV. RHEOLOGY OF GRANULAR POISEUILLE FLOW

The momentum transfer at particle level manifests at the macroscopic level as continuum stresses. The total stress ten-

sor has two components: "kinetic" stress and "collisional" stress. While the momentum transfer due to streaming motion of particles contributes to kinetic stress, the momentum transfer due to particle collisions contributes to collisional stress. In this section we present results for various rheological quantities such as shear stress, pressure, viscosity, and first normal stress difference. As discussed in Sec. III, all mean field quantities vary across the channel width, and hence the measurement of rheological quantities (pressure, shear stress, and viscosity) must be done via *binwise* averaging by dividing the channel width into a number of bins.

With $\tilde{W}$, $\tilde{W}/\tilde{g}$, $(\tilde{W}\tilde{g})^{1/2}$, and $\tilde{m}$ as the reference length, time, velocity, and mass, respectively, the relevant dimensionless quantities are

$$d = \frac{\tilde{d}}{\tilde{W}}, \quad t = \frac{\tilde{t}}{(\tilde{W}/\tilde{g})^{1/2}}, \quad \mathbf{C} = \frac{\tilde{\mathbf{C}}}{(\tilde{g}\tilde{W})^{1/2}},$$

$$\mathbf{P} = \frac{\tilde{\mathbf{P}}}{(\tilde{\rho}_p \tilde{g}\tilde{W})}, \quad T = \frac{\tilde{T}}{\tilde{g}\tilde{W}}, \quad \mu = \frac{\tilde{\mu}}{\tilde{\rho}_p \tilde{g}^{1/2}\tilde{W}^{3/2}}, \tag{11}$$

where $\tilde{\mathbf{C}}$ is the fluctuation (peculiar) velocity, $\tilde{\rho}_p$ the material density of particles, $\mathbf{P}$ the stress tensor, T the granular energy, and μ the shear viscosity.

Since the kinetic stresses arise due to the streaming motion of the particles, the expression for kinetic stress tensor is given by

$$\tilde{\mathbf{P}}_k = \tilde{m}_b \frac{\langle \tilde{\mathbf{C}}_i \otimes \tilde{\mathbf{C}}_i \rangle}{(\tilde{d}y)(\tilde{L})} = \frac{n_b \frac{\pi}{4}\tilde{\rho}_p \tilde{d}^2}{(\tilde{d}y)(\tilde{L})} \langle \tilde{\mathbf{C}}_i \otimes \tilde{\mathbf{C}}_i \rangle = \nu_b \tilde{\rho}_p \tilde{g}\tilde{W} \langle \mathbf{C}_i \otimes \mathbf{C}_i \rangle$$

$$\Rightarrow \mathbf{P}^k = \frac{\tilde{\mathbf{P}}_k}{(\tilde{\rho}_p \tilde{g}\tilde{W})} = \nu_b \langle \mathbf{C}_i \otimes \mathbf{C}_i \rangle, \tag{12}$$

where $\tilde{m}_b$ is the binwise mass of the granular fluid, ν_b is binwise volume fraction, $(\tilde{L}\tilde{d}y)$ is the area of each bin, and $\langle \cdots \rangle$ denotes binwise averaging over collisions.

Our interest is in the rapid flow regime where the particle collisions are assumed to be instantaneous and binary. The momentum change during a collision is given by the expression for collisional impulse $\tilde{I}$:

$$\tilde{\mathbf{I}} = \tilde{m} \frac{1 + e_n}{2} (\tilde{\mathbf{c}}_{12} \cdot \mathbf{k}) \mathbf{k}, \tag{13}$$

where $\mathbf{k}$ is the unit vector along the line of contact from particle 1 to particle 2. Hence the collisional stress due to this momentum exchange can be expressed as

$$\tilde{\mathbf{P}}^c = \frac{\tilde{d}}{\tau_d} \sum_{bin} \frac{\tilde{\mathbf{I}} \otimes \mathbf{k}}{(\tilde{L}\tilde{d}y)} = \left(\frac{\pi}{4}\right) [\tilde{\rho}_p \tilde{g}\tilde{W}] \left[\frac{d^3}{\tau_d (Ldy)}\right] \sum_{bin} \mathbf{I} \otimes \mathbf{k}$$

$$\Rightarrow \mathbf{P}^c = \frac{\tilde{\mathbf{P}}^c}{(\tilde{\rho}_p \tilde{g}\tilde{W})} = \left(\frac{\pi}{4}\right) \left[\frac{d^3}{\tau_d (Ldy)}\right] \sum_{bin} \mathbf{I} \otimes \mathbf{k}, \tag{14}$$

where τ_d is the duration of the averaging time window and the sum is taken over all collisions during τ_d. Note that kinetic stress (12) involves only bin averaging whereas collisional stress (14) involves both bin and time averaging. At low densities the kinetic stress is dominant since the collision rate is small and the mean free path of particles is large, whereas at high densities the collisional stress is dominant since the collision rate is large and the mean free path is small.

The total stress can be decomposed into an isotropic part and a stress deviator:

$$\mathbf{P} = \mathbf{P}^k + \mathbf{P}^c = p\mathbf{1} + \mathbf{\Pi}, \tag{15}$$

where p is the pressure, $\mathbf{\Pi}$ is the stress deviator, and $\mathbf{1}$ is the unit tensor. From the off-diagonal components of the deviatoric stress, we can calculate the *shear viscosity* which relates the rate of strain to the shear stress:

$$\mu = -\Pi_{xy}/\frac{du}{dy}. \tag{16}$$

The diagonal components of the stress deviator could be different from zero leading to an anisotropic stress tensor. This stress anisotropy can be quantified by the first normal stress difference [13]

$$\mathcal{N}_1 = \frac{\Pi_{xx} - \Pi_{yy}}{p}. \tag{17}$$

Note that this quantity is scaled by pressure to obtain its relative magnitude with respect to pressure. For a Newtonian fluid $\mathcal{N}_1 = 0$ and a nonzero $\mathcal{N}_1$ indicates the non-Newtonian character of the fluid.

A. Theoretical expressions for rheological quantities

The theoretical expressions for viscosity, shear stress, and pressure for identical, rough, inelastic, and circular disks were derived from dense-gas kinetic theory by Jenkins and Richman [11]. For quasielastic collisions ($e_n \sim 1$) of smooth particles, these expressions reduce to the forms given below.

For a Navier-Stokes-order constitutive model, the total stress is given by

$$P_{\alpha\beta} = p\delta_{\alpha\beta} + \Pi_{\alpha\beta}, \tag{18}$$

where p is the pressure (in dimensionless form)

$$p \equiv \nu T(1 + 2G) \tag{19}$$

and $\Pi_{\alpha\beta}$ is the shear stress which, for our unidirectional Poiseuille flow, reduces to

$$\Pi_{xy} = -\mu \frac{dU_x}{dy}. \tag{20}$$

The dimensionless expression for the shear viscosity, μ, is

$$\mu \equiv (T/4\pi)^{1/2} [(8/\pi)G + (G^{-1} + 2 + G)]. \tag{21}$$

In the above expressions, $G \equiv \nu\chi$, ν is the volume fraction, and χ is the radial distribution function for disks at contact,

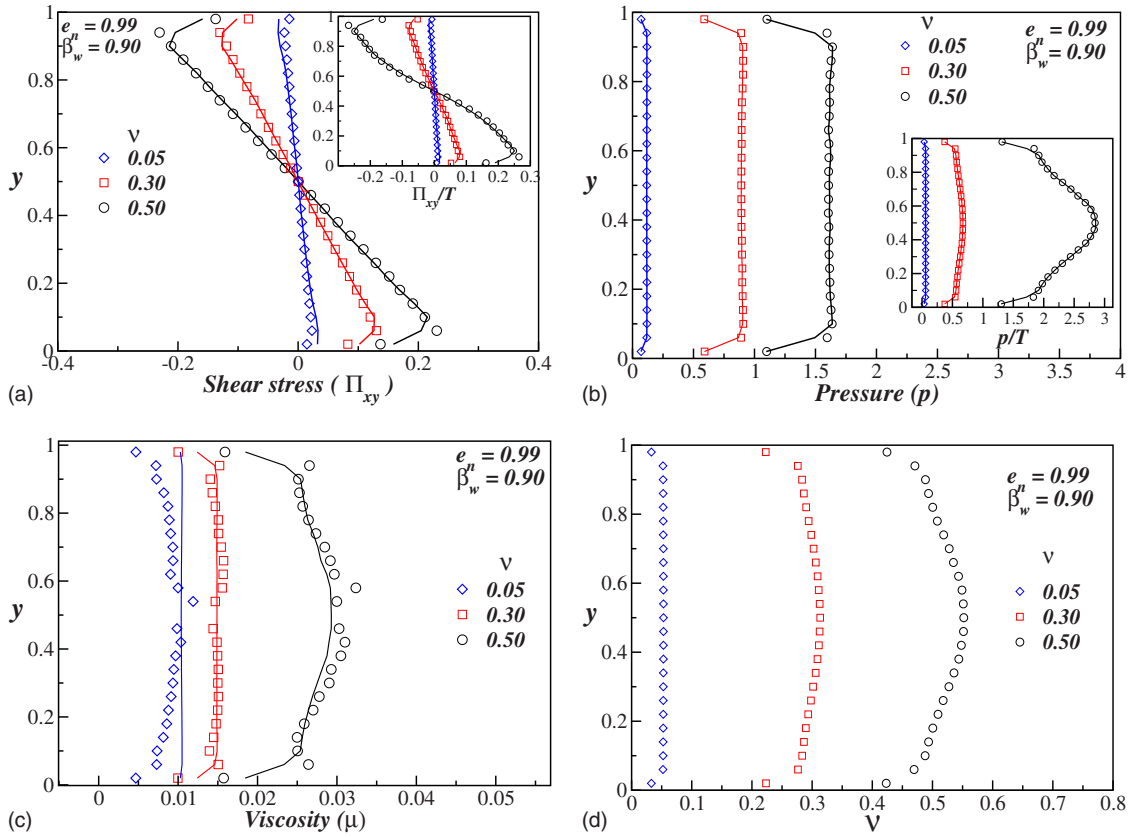

FIG. 11. (Color online) Variations in (a) shear stress, (b) pressure, (c) viscosity, and (d) particle volume fraction across the width of the channel for a smooth wall (β_w=0.9) with quasielastic collisions (e_n=0.99). The symbols represent simulation data and continuous lines represent theoretical results.

$$\chi(\nu) = \frac{1 - \frac{7}{16}\nu}{(1-\nu)^2}. \tag{22}$$

We substitute the granular temperature, volume fraction, and velocity profiles from our simulations into the above equations to obtain theoretical predictions for shear stress, pressure, and viscosity as functions of y coordinate.

B. Comparison of simulation and theory

In this section, we compare our simulation data on pressure, shear stress, and viscosity with the prediction of Eqs. (19)–(21), respectively. All simulations were performed by fixing the particle number at N=900 and the channel width at W/d=31 with 24 bins across the channel width.

A comparison of simulation (symbols) and theoretical (continuous lines) results in the quasielastic limit (e_n=0.99) for smooth walls (β_w=0.9) is shown in Fig. 11 and the results for rough walls (β_w=0.1) are shown in Fig. 12; the results for three values of mean particle volume fractions (ν=0.05, 0.3, and 0.5) are shown. The shear stress and pressure profiles scaled by the granular temperature (i.e., $\Pi_{xy}/\sqrt{T}$ and p/T) are displayed in the inset of respective plots. There is a good agreement between simulation and theory over a wide range of densities. Changing the wall roughness (β_w =0.9 and 0.1) does not seem to affect the degree of agreement between simulation and theory as observed from a comparison of Figs. 11 and 12. The profiles of particle volume fraction at different mean volume fractions are shown in Figs. 11(d) and 12(d). An increase in the average volume fraction enhances the gradients of density along y direction, which is an indication of clustering of particles around the center of the channel. From the corresponding profiles of granular temperature (not shown), we find that the temperature is lower at denser regions around the centerline and higher at dilute regions near the walls.

The effects of restitution coefficient (e_n) on rheological quantities are presented in Figs. 13(a)–13(d) for which the wall roughness is set to β_w=0.9 with e_n=0.9. From the plots of shear stress and pressure in Figs. 13(a) and 13(b), it is clear that the discrepancies between the theoretical and simulation results become appreciable only at moderate and high densities, and the agreement is reasonably good at low density (ν=0.05). The latter observation is surprising since the flow is much beyond the Navier-Stokes regime (holds for Kn$<$0.01) when the density is low ($\nu<$0.2, see Fig. 6). The density profiles in Fig. 13 indicate the formation of a dense plug around the center of the channel for $\nu\sim$0.5 and the viscosity profile shows a divergence in the plug region. The discrepancies between simulation and theory are further enhanced at e_n=0.8 as seen in Fig. 14. The results remain qualitatively similar for rough walls (e.g., at β_w=0.1, not shown).

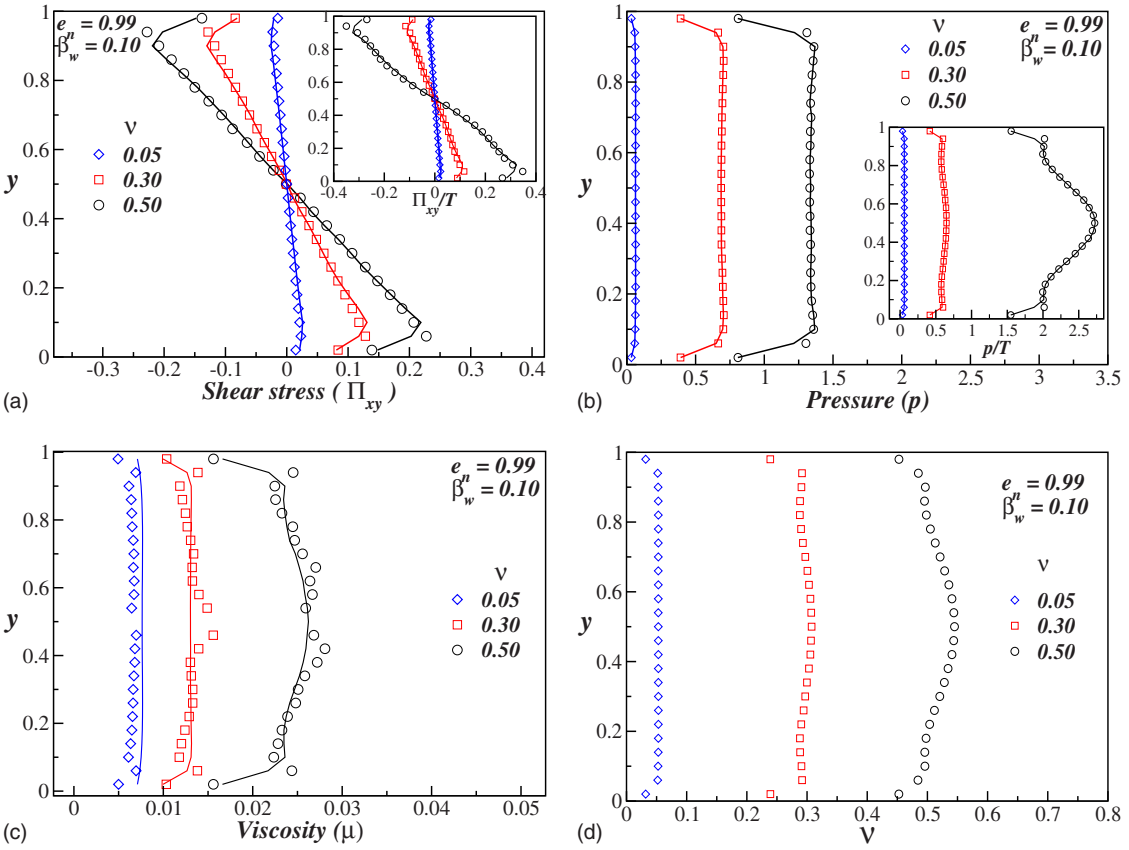

FIG. 12. (Color online) Same as Fig. 11, but for a rough wall (β_w=0.1).

On the whole, we find excellent agreement between simulation and theory for pressure, shear stress, and viscosity when the particle collisions are nearly elastic ($e_n \sim 1$) and this agreement deteriorates significantly with increasing dissipation levels. This observation is expected since Navier-Stokes'-order constitutive model [11] is strictly valid for $e_n \sim 1$ at low Knudsen numbers (Kn$\sim$0). One interesting and unexpected finding is that, even in the slip-flow ($0.01 <$ Kn < 0.1) and transitional-flow ($0.1 <$ Kn < 1) regimes of Knudsen number, the theory predicts the simulation data nicely for $e_n \sim 1$. Changing the wall roughness (β_w) does not seem to affect the above findings. It is interesting to recall from our recent work [9] that the local velocity distribution functions in GPF remains a Gaussian for a wide range of densities at quasielastic collisions ($e_n \sim 1$) even when the Knudsen number is of order 1.

C. First normal stress difference

The first normal stress difference $\mathcal{N}_1$, Eq. (17), is a measure of the degree of non-Newtonian character of the fluid. The origin of $\mathcal{N}_1$ in the dilute limit has been tied to the Burnett-order corrections to the Boltzmann equation and is universally present in a molecular gas [12]. While the magnitude of $\mathcal{N}_1$ is negligibly small in a molecular gas, it is a measurable quantity in granular gases, with inelasticity being the amplifier of $\mathcal{N}_1$. In the dense limit, however, the origin of $\mathcal{N}_1$ has been tied to "collisional" anisotropy [13]. In this section, we analyze the behavior of $\mathcal{N}_1$ in GPF which has not been quantified before.

Figures 15(a) and 15(b) show the profiles of $\mathcal{N}_1$ at different mean volume fractions for restitution coefficients of e_n =0.99 and 0.8, respectively, with a wall roughness of β_w =0.9 (smooth wall). The corresponding results for a rough wall (β_w=0.1) are qualitatively similar and hence not shown. The magnitude of $\mathcal{N}_1$ is very small for e_n=0.99 over a wide range of volume fractions; this is expected since the granular fluid behaves like a Newtonian fluid for quasielastic collisions ($e_n \sim 1$). The magnitude of $\mathcal{N}_1$ increases with increasing dissipation (e_n=0.8) as in Fig. 15(b). Further, $\mathcal{N}_1$ has a *nonmonotonic* variation with density: initially $\mathcal{N}_1$ increases at low densities, reaches a maximum value at some moderate density, and then decreases with further increase in density. Interestingly, $\mathcal{N}_1$ *changes* its sign near the channel centerline beyond some critical density. For example, at ν=0.5 and e_n =0.8, the first normal stress difference is negative around the channel centerline as seen in Fig. 15(b).

To get a better picture of the *negative* first normal stress difference, we shift our focus to the centerline region of the channel where the density is relatively larger. In Fig. 16, the effect of mean particle volume fraction on the first normal stress difference at the channel centerline (i.e., the value of $\mathcal{N}_1$ at the central bin positioned around y=0.5) is shown. It is observed that $\mathcal{N}_1$ varies nonmonotonically with mean volume fraction and reverses its sign at a critical density depending on the value of e_n. The inset of Fig. 16 displays $\mathcal{N}_1$ as a function of the "local" (binwise) volume fraction at the

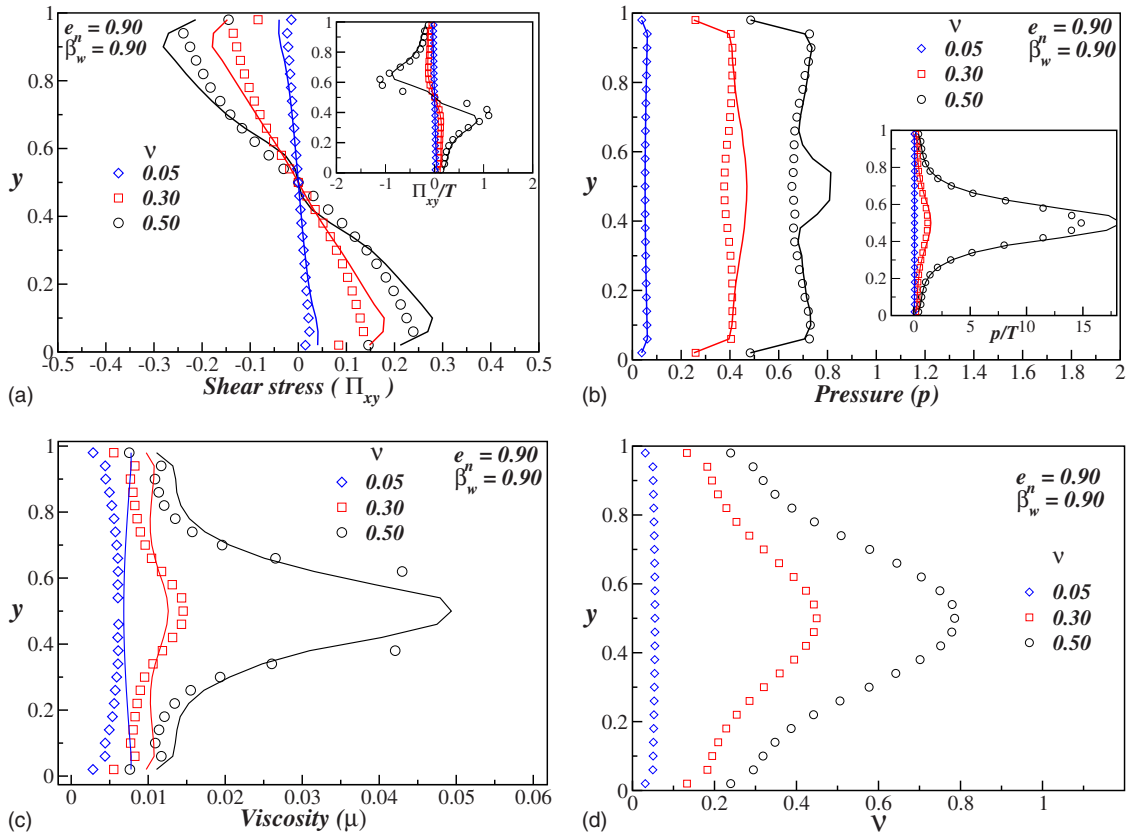

FIG. 13. (Color online) Same as Fig. 11, but for a restitution coefficient of e_n=0.9.

central bin; since the system is inhomogeneous, the variation in $\mathcal{N}_1$ with the local volume fraction is more meaningful. From the inset of Fig. 16, we find that decreasing the restitution coefficient increases the critical density above which $\mathcal{N}_1$ is negative. The latter observation is similar to the findings of Alam and Luding [13–15] for the simple shear flow. However, the nonmonotonic variation in $\mathcal{N}_1$ at lower densities is different in granular Poiseuille flow and has not been reported before. Another noteworthy point is that the overall variation in $\mathcal{N}_1$ with density and the critical density for the sign reversal of $\mathcal{N}_1$ do not depend on the wall roughness (compare open and solid symbols for β_w=0.1 and 0.9, respectively, in Fig. 16).

The *sign reversal* of first normal stress difference $\mathcal{N}_1$ was first reported by Alam and Luding [13] in a sheared granular fluid. By decomposing $\mathcal{N}_1$ into two parts,

$$\mathcal{N}_1 = \mathcal{N}_1^k + \mathcal{N}_1^c = \frac{\Pi_{xx}^k - \Pi_{yy}^k}{p} + \frac{\Pi_{xx}^c - \Pi_{yy}^c}{p}, \tag{23}$$

they showed that the kinetic component of first normal stress difference, $\mathcal{N}_1^k$, is maximum in the dilute limit and decays to zero at high volume fractions, whereas its collisional part, $\mathcal{N}_1^c$, is a nonmonotonic function of density, which increases from zero in the dilute limit, reaches a maximum value at some intermediate density and then decreases, attaining a

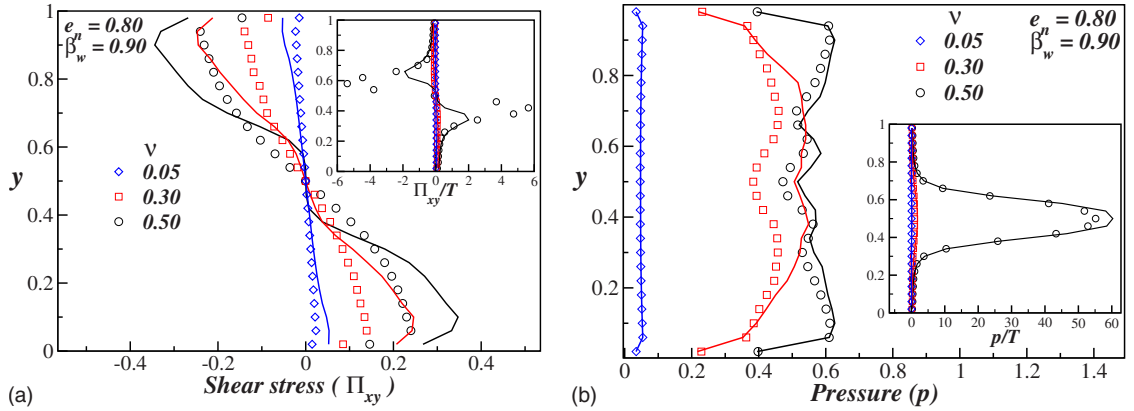

FIG. 14. (Color online) Same as Fig. 11, but for a restitution coefficient of e_n=0.8.

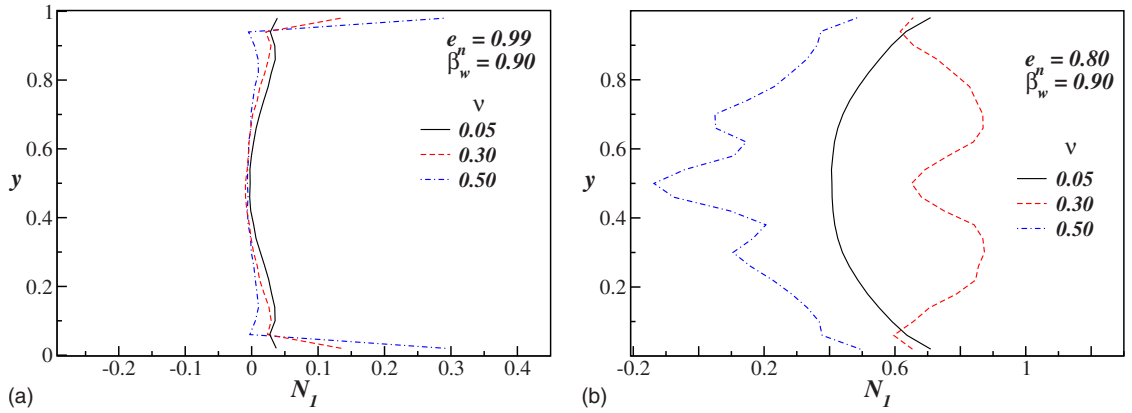

FIG. 15. (Color online) Profiles of the first normal stress difference across the channel width for (a) e_n=0.99 and (b) e_n=0.8 with a smooth wall (β_w=0.9) at different mean volume fractions.

negative value above a critical density depending on the coefficient of restitution. They further showed that, in the dilute limit, the total normal stress difference follows the behavior of $\mathcal{N}_1^k$ but at high densities its behavior is dictated by $\mathcal{N}_1^c$. The reversal in the sign of $\mathcal{N}_1^c$ was subsequently tied to a preferred value of the collision angle which is a direct consequence of the microstructural reorganization of particles in the dense limit. This explains the sign reversal of $\mathcal{N}_1$ in the dense sheared granular fluid.

We take a similar approach here to understand the origin of *negative* first normal stress difference in granular Poiseuille flow. In Figs. 17(a) and 17(b), the kinetic and collisional components of $\mathcal{N}_1$, respectively, are shown for different densities at e_n=0.8 with smooth walls (β_w=0.9); similar results for rough walls (β_w=0.1) are displayed in Fig. 18. We see that both $\mathcal{N}_1^k$ and $\mathcal{N}_1^c$ vary nonmonotonically with increasing mean volume fraction (except near two walls). In GPF $\mathcal{N}_1^k$ attains its maximum at some intermediate density which is in contrast to the simple shear flow (Alam and Luding [13]) for which $\mathcal{N}_1^k$ in the dilute limit ($\nu \to 0$). In the dense limit, however, $\mathcal{N}_1^k$, at the channel centerline, decays to zero [Figs. 17(a) and 18(a)] since the streaming motion of particles becomes negligible at large enough densities. However, the collisional component of $\mathcal{N}_1$ increases from zero in the dilute limit, reaches a maximum positive value at some intermediate value of ν, and then decreases with further increase in density and reverses its sign beyond a critical volume fraction [Figs. 17(b) and 18(b)]. Therefore, the origin of "sign reversal" of $\mathcal{N}_1$ in GPF is tied to the sign reversal of $\mathcal{N}_1^c$ as in the simple shear flow (Alam and Luding [13]).

The sign reversal of $\mathcal{N}_1$ can be concisely presented in the form of a phase diagram in the (ν_{bin}, e_n) and (ν, e_n) planes as shown in Figs. 19(a) and 19(b), respectively. Note that the ordinate in Fig. 19(a) is ν_{bin} that corresponds to the "local" particle volume fraction in the central bin, but the ordinate in Fig. 19(b) corresponds to the mean particle volume fraction. In each phase diagram, the solid line with black circles indicates the zeros of $\mathcal{N}_1$ and the dashed line with cross marks indicates the zeros of $\mathcal{N}_1^c$; each line demarcates the regions of positive (below) and negative (above) normal stress differences. In Figs. 19(a) and 19(b), we note that the zero lines of $\mathcal{N}_1$ and $\mathcal{N}_1^c$ coincide with each other at lower values of $e_n \leq 0.8$, but deviate from each other at higher e_n. This deviation becomes noticeable for $e_n \geq 0.9$, with $\mathcal{N}_1^c$ attaining a zero at a lower volume fraction compared to $\mathcal{N}_1$. If the sign re-

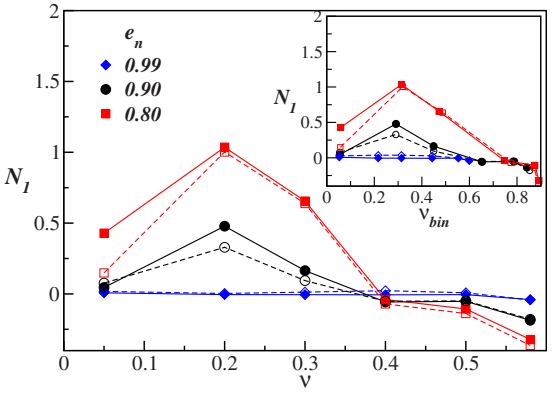

FIG. 16. (Color online) Variation in the first normal stress difference (at the channel centerline) with mean volume fraction for e_n=0.8 and 0.9. In the inset $\mathcal{N}_1$ is plotted against the local volume fraction or the bin volume fraction. The filled symbols represent smooth walls (β_w=0.9) and open symbols represent rough walls (β_w=0.1).

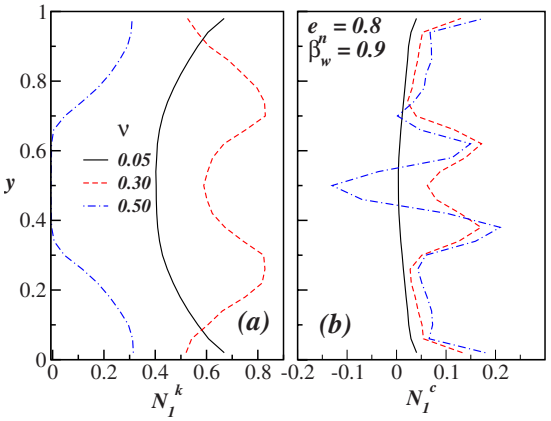

FIG. 17. (Color online) Profiles of (a) kinetic component $\mathcal{N}_1^k$ and (b) collisional component $\mathcal{N}_1^c$ of first normal stress difference across the channel at e_n=0.8 and different average volume fractions for smooth walls (β_w=0.9).

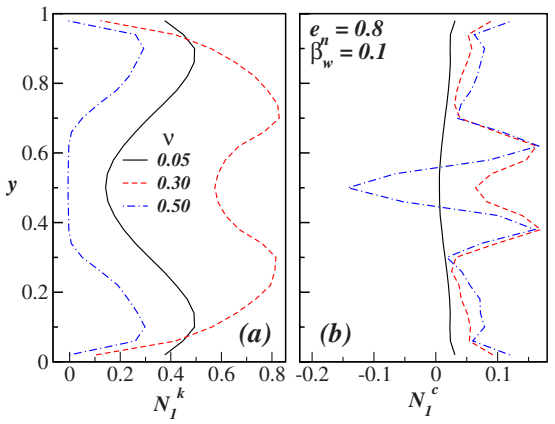

FIG. 18. (Color online) Same as Fig. 17, but for a rough wall (β_w=0.1).

versal of $\mathcal{N}_1$ is solely due to that of $\mathcal{N}_1^c$, both solid and dashed lines in Fig. 19 would have coincided with each other.

To find out the reason for the deviation between the zero lines of $\mathcal{N}_1$ and $\mathcal{N}_1^c$ for quasielastic collisions, we show an analog of Fig. 16 for $\mathcal{N}_1^c$ in Fig. 20; parameter values are same as in Fig. 18. At e_n=0.8, the variation in $\mathcal{N}_1^c$ with volume fraction looks qualitatively similar to that of $\mathcal{N}_1$ and its zero-crossing volume fraction is almost the same as that for $\mathcal{N}_1$ (see Fig. 16). In contrast to the nonmonotonic variation in $\mathcal{N}_1$ with ν and ν_{bin} at e_n, its collisional component $\mathcal{N}_1^c$ at e_n =0.9 decays monotonically with both ν and ν_{bin}; $\mathcal{N}_1^c$ has a small negative value over a range of mean volume fractions ($\nu \sim 0.3-0.5$) and becomes of significant magnitude only at large volume fractions ($\nu \sim 0.6$). Similar observations could be made from the inset of Fig. 20, where $\mathcal{N}_1^c$ is presented as a function of the local volume fraction ν_{bin}. Clearly, the finite positive values for the kinetic component of $\mathcal{N}_1$, $\mathcal{N}_1^k$, at lower volume fractions make the zero crossings of the total normal stress difference, $\mathcal{N}_1=\mathcal{N}_1^k+\mathcal{N}_1^c$, at a relatively larger volume fraction than that for $\mathcal{N}_1^c$ as depicted in Fig. 19.

From the above discussion, we conclude that the origin of sign reversal of $\mathcal{N}_1$ in GPF is the same (i.e., the sign change of its collisional component) as in the simple shear flow [13–15]. However, unlike in simple shear flow, this sign reversal can occur even at a modest density in GPF for quasielastic collisions. This latter observation is possibly due to the nonmonotonic variation in $\mathcal{N}_1^k$ with density in GPF.

V. SUMMARY AND CONCLUSION

We have investigated the slip velocity and the stresses in the gravity-driven granular Poiseuille flow (GPF) using event-driven simulations in the rapid flow regime of dilute to dense flows. The well-known "inelastic" smooth hard-disk model, characterized by normal restitution coefficient (e_n), has been used to model particle-particle collisions. The wall roughness, characterizing the frictional properties of walls, has been modeled by specifying a single parameter, β_w, the tangential restitution coefficient for wall-particle collisions.

It is shown that the slip velocity (U_w) and its gradient (dU_w/dy) depend on the wall roughness, the mean particle volume fraction, and the normal restitution coefficient. In particular, the slip velocity decreases sharply with increasing wall roughness and mean particle volume fraction, but decreases mildly with increasing inelastic dissipation in the intermediate range of Knudsen number, $\mathrm{Kn} \in (0.05, 1)$. The gradient of slip velocity is found to follow a single power-law relation with Knudsen number, $(dU_w/dy) \propto \mathrm{Kn}^{-\alpha_2}$, for the whole studied range of $\mathrm{Kn} \in (0, 3)$. In contrast, the variation in slip velocity with Kn shows three distinct regimes in terms of Knudsen number: (i) U_w is independent of Kn for $\mathrm{Kn} < 0.05$; (ii) $U_w \propto \mathrm{Kn}^{\gamma(e_n)}$ for $\mathrm{Kn} \in (0.05, 1)$; (iii) $U_w \propto \mathrm{Kn}^{0.37}$ for $\mathrm{Kn} > 1$. A qualitative comparison of our results with a heuristic theory for the slip velocity [22] shows that the specularity coefficient (or the tangential momentum accommodation coefficient) depends not only on the wall roughness (β_w) but also on particle (e_n) and flow (ν) parameters. Since the Knudsen number depends on β_w, e_n, and ν, it is suggested that a Knudsen-number-dependent specularity coefficient could be determined from simulations.

The rheological quantities such as pressure, shear stress, viscosity, and first normal stress difference of granular Poiseuille flow have been obtained at various densities. In the quasielastic limit ($e_n \sim 1$), the simulation results agree well with expressions derived from kinetic theory by Jenkins and Richman [11] for circular disks. As the level of inelastic

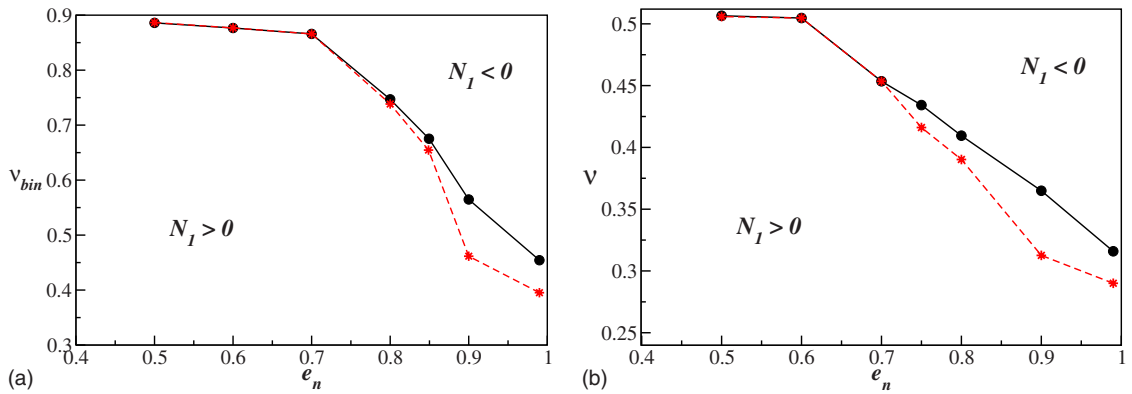

FIG. 19. (Color online) Phase diagrams showing the regions of positive and negative first normal stress difference, $\mathcal{N}_1$, in the (a) (ν_{bin}, e_n) plane and (b) (ν, e_n) plane. The solid line indicates $\mathcal{N}_1$=0 and the dashed line $\mathcal{N}_1^c$=0.

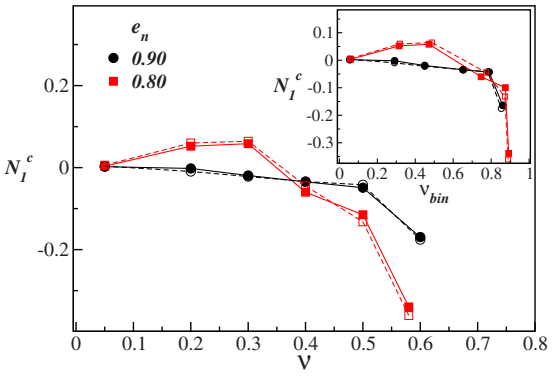

FIG. 20. (Color online) Variation in the collisional component of first normal stress difference at the channel centerline with mean volume fraction for e_n=0.8 and 0.9. In the inset $\mathcal{N}_1^c$ is plotted against the local volume fraction at the channel centerline. The filled symbols represent smooth walls (β_w=0.9) and open symbols represent rough walls (β_w=0.1).

dissipation increases the simulation results deviate from theoretical predictions, which is expected since the theory has been developed for quasielastic collisions. The first normal stress difference ($\mathcal{N}_1$) is negligible in the quasielastic limit but displays nonmonotonic variation with the particle volume fraction at higher dissipations. Near the centerline of the channel where the granular fluid is relatively denser, $\mathcal{N}_1$ increases from zero in the dilute limit, reaches a maximum at some intermediate density, and then decreases, attaining a negative value beyond some critical density. Probing the kinetic ($\mathcal{N}_1^k$) and collisional ($\mathcal{N}_1^c$) components of $\mathcal{N}_1$ reveals that the behavior of $\mathcal{N}_1$ at large densities is dictated by the behavior of its collisional component ($\mathcal{N}_1^c$), which reverses sign beyond a certain density due to the structural reorganization of particles. Therefore, the origin of the sign reversal of $\mathcal{N}_1$ in GPF is the same as in the dense plane shear flow of granular materials [13]. In contrast to the plane shear case [13], this sign reversal in GPF can occur even at a much lower particle volume fraction if the particle collisions are quasielastic.

The present results on the non-Newtonian rheology of GPF clearly indicate the shortcomings of the kinetic-theory models for rapid granular flows. All kinetic-theory models [12] predict that $\mathcal{N}_1$ is maximum in the dilute limit and decreases monotonically to zero in the dense limit. These theories are not able to predict the *sign reversal* of $\mathcal{N}_1$ for dense flows; clearly, the Burnett-order corrections for dense flows are inadequate to resolve this important issue. Moreover, we have found that $\mathcal{N}_1$ can change sign in GPF at a much lower density (than in plane shear flow) for quasielastic collisions. Therefore, the use of Navier-Stokes-order continuum theory even at a modest density needs to be critically judged for GPF. Since the origin of the sign reversal of $\mathcal{N}_1$ in GPF is the same as in shear flow, we suggest that the collisional anisotropy [13] must be incorporated in kinetic-theory models.

[1] S. B. Savage, Adv. Appl. Mech. **24**, 289 (1984); H. J. Herrmann, J.-P. Hovi, and S. Luding, *Physics of Dry Granular Media* (Kluwer Academic, Dordrecht, 1998); Y. Forterre and O. Pouliquen, Annu. Rev. Fluid Mech. **40**, 1 (2008).

[2] C. S. Campbell, Annu. Rev. Fluid Mech. **22**, 57 (1990); I. Goldhirsch, *ibid.* **35**, 267 (2003); T. Pöschel and S. Luding, *Granular Gas* (Springer, Heidelberg, 2001).

[3] H. M. Jaeger, S. R. Nagel, and R. Behringer, Rev. Mod. Phys. **68**, 1259 (1996); L. P. Kadanoff, *ibid.* **71**, 435 (1999); I. Aranson and L. S. Tsimring, *ibid.* **78**, 641 (2006).

[4] S. B. Savage and D. J. Jeffrey, J. Fluid Mech. **110**, 255 (1981); P. K. Haff, *ibid.* **134**, 401 (1983); J. T. Jenkins and S. B. Savage, *ibid.* **130**, 187 (1983); N. Sela and I. Goldhirsch, *ibid.* **361**, 41 (1998); J. M. Montanero, V. Garzo, A. Santos, and J. J. Brey, *ibid.* **389**, 391 (1999); V. Kumaran, *ibid.* **561**, 1 (2006); M. Alam, J. T. Willits, B. Ö. Arnarson, and S. Luding, Phys. Fluids **14**, 4085 (2002).

[5] R. A. Bagnold, Proc. R. Soc. London, Ser. A **225**, 49 (1954).

[6] N. Menon and D. J. Durian, Science **275**, 1920 (1997); G. Reydellet, F. Rioual, and E. Clement, Europhys. Lett. **51**, 27 (2000); J.-C. Tsai, W. Losert, G. A. Voth, and J. P. Gollub, Phys. Rev. E **65**, 011306 (2001); I. Zuriguel, A. Garcimartin, D. Maza, L. A. Pugnaloni, and J. M. Pastor, *ibid.* **71**, 051303 (2005); J. Choi, A. Kudrolli, R. R. Rosales, and M. Z. Bazant, Phys. Rev. Lett. **92**, 174301 (2004); S. Moka and P. R. Nott, *ibid.* **95**, 068003 (2005).

[7] G. Peng and H. J. Herrmann, Phys. Rev. E **49**, R1796 (1994); T. Pöschel, J. Phys. **4**, 449 (1994); T. Raafat, J. P. Hulin, and H. J. Herrmann, Phys. Rev. E **53**, 4345 (1996); O. Baran D. Erta, and T. C. Halsey, *ibid.* **74**, 051302 (2006).

[8] E. Liss, S. Conway, and B. J. Glasser, Phys. Fluids **14**, 3309 (2002).

[9] K. C. Vijayakumar and M. Alam, Phys. Rev. E **75**, 051306 (2007).

[10] C. Denniston and H. Li, Phys. Rev. E **59**, 3289 (1999); A. Ferguson and B. Chakraborty, *ibid.* **73**, 011303 (2006).

[11] J. T. Jenkins and M. W. Richman, Phys. Fluids **28**, 3485 (1985).

[12] I. Goldhirsch and N. Sela, Phys. Rev. E **54**, 4458 (1996).

[13] M. Alam and S. Luding, Phys. Fluids **15**, 2298 (2003).

[14] M. Alam and S. Luding, *Powders and Grains 2005*, edited by R. Garcia-Rojo *et al.* (Balkema, The Netherlands, 2005), p. 1141.

[15] M. Alam and S. Luding, Phys. Fluids **17**, 063303 (2005).

[16] B. D. Lubachevsky, J. Comput. Phys. **94**, 255 (1991).

[17] J. Koplik and J. Banavar, Annu. Rev. Fluid Mech. **27**, 257 (1995).

[18] M. P. Allen and D. J. Tildesley, *Computer Simulation of Liquids* (Oxford University Press, Oxford, 1987).

[19] See EPAPS Document No. E-PLEEE8-80-016908 for supplementary materials containing two *movies* of GPF at a mean density ν=0.56, with other parameters as in Fig. 2; both movies are in avi-format at low resolution. Particles are almost uniformly distributed in *movie 1* for e_n=0.99, but they form a

dense plug around the centerline in *movie 2* for e_n=0.8. The flow is from left to right. For more information on EPAPS, see http://www.aip.org/pubservs/epaps.html.

[20] J. C. Maxwell, Philos. Trans. R. Soc. London **170**, 231 (1879).

[21] G. Kaniadakis and A. Beshok, *Micro Flows: Fundamentals and Simulation* (Springer, New York, 2001); E. P. Muntz, Annu. Rev. Fluid Mech. **21**, 387 (1989).

[22] K. Hui, P. K. Haff, J. E. Ungar, and R. Jackson, J. Fluid Mech. **145**, 223 (1984).

[23] J. T. Jenkins and M. W. Richman, J. Fluid Mech. **171**, 53 (1986).

[24] S. B. Savage and M. Sayed, J. Fluid Mech. **142**, 391 (1984); P. C. Johnson and R. Jackson, *ibid.* **176**, 67 (1987); M. Alam and P. R. Nott, *ibid.* **377**, 99 (1998); J.-C. Tsai, G. A. Voth, and J. P. Gollub, Phys. Rev. Lett. **91**, 064301 (2003); M. Alam *et al.*, J. Fluid Mech. **523**, 277 (2005).

[25] S. Chapman and T. G. Cowling, *The Mathematical Theory of Non-Uniform Gases* (Cambridge University Press, Cambridge, England, 1970).